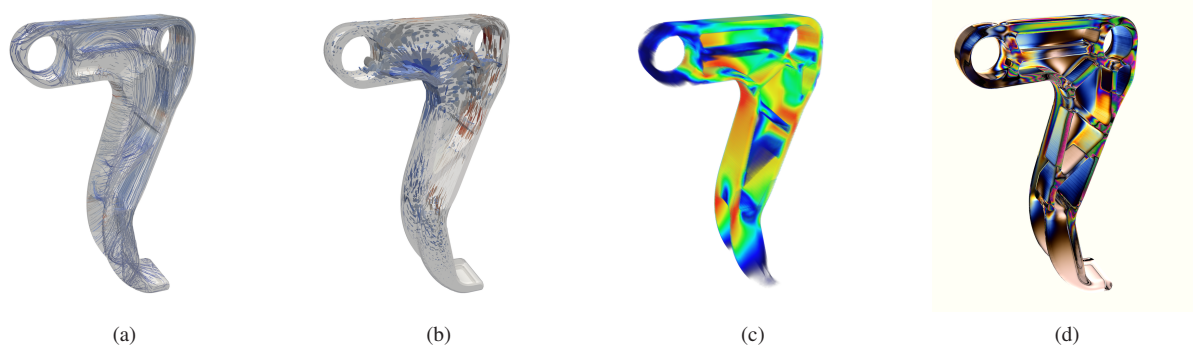


# Photoelasticity Raycasting

M. Bußler<sup>1</sup>, T. Ertl<sup>1</sup>, and F. Sadlo<sup>2</sup>

<sup>1</sup>University of Stuttgart, Germany

<sup>2</sup>Heidelberg University, Germany



**Figure 1:** Brake Lever dataset. Tensor field lines (a) are continuous but not quantitative. Superquadric glyphs (b) are quantitative but discrete. Von Mises stress rendering (c) is continuous but not showing orientation. Our virtual photoelasticity (d), which corresponds to experimental stress analysis with polariscopes, is continuous, quantitative, and conveys orientation.

## Abstract

We present a novel physically-based method to visualize stress tensor fields. By incorporating photoelasticity into traditional raycasting and extending it with reflection and refraction, taking into account polarization, we obtain the virtual counterpart to traditional experimental polariscopes. This allows us to provide photoelastic analysis of stress tensor fields in arbitrary domains. In our model, the optical material properties, such as stress-optic coefficient and refractive index, can either be chosen in compliance with the subject under investigation, or, in case of stress problems that do not model optical properties or that are not transparent, be chosen according to known or even new transparent materials. This enables direct application of established polariscope methodology together with respective interpretation. Using a GPU-based implementation, we compare our technique to experimental data, and demonstrate its utility with several simulated datasets.

Categories and Subject Descriptors (according to ACM CCS): I.6.6 [Simulation and Modeling]: Simulation Output Analysis—; I.3.7 [Computer Graphics]: Three-Dimensional Graphics and Realism—;

## 1. Introduction

Tensor fields are ubiquitous in science and engineering, and there has been considerable research on their adequate visualization. Whereas scalar fields are often amenable to color-based visualization, and visualization of vector fields can employ contrast to convey direction, such direct perceptual representations are not available for tensor data.

Part of the existing techniques for tensor field visualization derive lower-dimensional quantities from the tensors and employ existing approaches for their visualization, which, however, involves some kind of projection and typically restricts the representation. Another, and widely used, discipline is concerned with the development of glyphs that convey the full information of tensors, however, with the

drawback that these representations typically lack continuity. The approach that we describe in this paper also takes the full tensor information into account, but produces continuous visualizations by means of a physically-based model.

In general, visualization results require interpretation, and this interpretation is primarily based on experience—experience regarding the problem domain where the data originated from, and, in particular, experience with the visualization technique itself. While straightforward visualization techniques tend to be easy to interpret, they often lack expressiveness. On the other hand, advanced visualization techniques often require substantial experience for appropriate interpretation and handling.

Self-illustrating phenomena are of interest in many regards. On the one hand, these natural visualizations readily reveal physical mechanisms and have been providing powerful analysis tools, particularly before the onset of scientific computing. On the other hand, they represent an excellent source for computational visualization techniques—by mimicking their effects with computational models, we obtain physically-based visualization techniques that are well-defined, can be compared with experiments, and, most important, make use of the interpretation experience gained from the real self-illustrating counterparts. Examples for such success stories in scientific visualization include volume rendering, line integral convolution, and dye advection. With this paper, we would like to call attention to the self-illustrating phenomenon of photoelasticity and advocate its application for computational visualization of indefinite symmetric tensor fields, i.e., in particular, stress tensor fields.

Photoelasticity is present if transparent materials exhibit birefringence, i.e., if they impose two different refractive indices on passing light. This can be due to anisotropic properties of the material itself, such as in the case of crystals, or caused by stresses in many transparent materials. Thus, the photoelastic effect is traditionally used in polariscopes (Figure 2) for the analysis of stresses in transparent objects. Depending on the type of polarization of their polarizers and analyzers, which may be linear or circular, the respective polariscopes are denoted plane polariscope and circular polariscope, respectively. In our approach, we model both variants for the analysis of stress fields. Note that we use the polariscope metaphor also for stress fields that were obtained in absence of optical considerations or for non-transparent objects, enabling the utilization of interpretation experience from experimental photoelasticity analysis to any stress field data. In such cases, the user is free to choose the optical properties, i.e., the refractive index and stress-optic coefficient.

Our contributions include:

- Photoelasticity for scientific visualization of stress fields.
- Incorporation of photoelasticity into raycasting, including refraction and reflection, and hence allowing for physically-based analysis of arbitrary 3D data.
- A GPU implementation providing interactive rates.

## 2. Related Work

There is a substantial amount of work on computer-aided photoelastic analysis [Pat02], which, however, is experimental and therefore not closely related to our work. We refer to textbooks on optics [Hec02] and solid mechanics [Sha08] for an introduction to the topic, to the manual by Doyle and Phillips [Kob83], and to the video [FM49] that served for validation of our technique. A recent example of photoelasticity applications is the work by Deuschle et al. [DWG\*06] in the context of generating ground truth for simulation data. Traditional photoelastic analysis (and hence also our approach) does not involve scattering. Nevertheless, the work by Chandrasekhar [Cha60] on the radiative transfer equation provides a good introduction to the topic of polarization.

In the field of raytracing, i.e., where optical effects are considered only at material interfaces, polarization is addressed by Wolff and Kurlander [WK90], birefringence in anisotropic media by McClain et al. [MHC93], birefringence in uniaxial media by Weidlich and Wilkie [WW08], and in biaxial media by Latorre et al. [LSG12]. Visualization of polarization in rendering is the subject of the work by Wilkie and Weidlich [WW10]. Combined rendering of polarization and fluorescence is addressed by Wilkie et al. [WTP01]. An overview of polarization in computer graphics can be found in the course notes by Wilkie and Weidlich [WW12]. All these works are related to ours in the sense that polarized light is traced, but none of these techniques involves continuous effects on light between the interfaces in terms of raycasting, as is necessary for our application.

We base our work on the model of integrated photoelasticity by Aben [Abe79]. In his (and subsequent) work, effects at interfaces are neglected, i.e., reflection and refraction are not addressed. It is our main contribution to include Aben's model into raycasting, extend it with reflection and refraction, and to advocate its use for the visualization of stress tensor fields in general. This enables us to provide at interactive frame rates a true virtual counterpart to experimental photoelastic analysis of arbitrarily-shaped 3D objects.

In contrast to the large body of literature on the visualization of semidefinite symmetric tensor fields, there is less work so far on visualization of indefinite symmetric fields. In the field of glyph-based visualization, the superquadric glyphs presented by Schultz and Kindlmann [SK10] are a primary choice for general second-order symmetric tensors. In the field of continuous visualization of tensor fields, widely used visualization techniques for general tensor fields include tensorlines by Weinstein et al. [WKL99], hyperstreamlines by Delmarcelle and Hesselink [DH93], and hue balls and lit tensors by Kindlmann and Weinstein [KW99]. It has to be noted that many visualization techniques focus on semidefinite symmetric tensors and that many of those are not directly applicable to indefinite symmetric tensor fields. One such example is fractional anisotropy [WPG\*97] and the techniques that utilize it. We refer the reader to

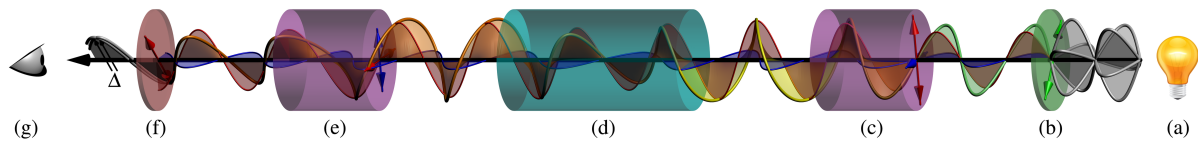


**Figure 2:** Circular polariscope, from right to left. Incident light (gray) is linearly polarized (green), and transformed to circular polarization (yellow) while passing a  $\lambda/4$ -plate (magenta, fast direction by red arrow, slow by blue). It then enters the material under investigation (blue), which, in general, renders it elliptically polarized (orange). Subsequently, it passes another  $\lambda/4$ -plate with opposite orientation, and from that, a single linear polarization is selected by the analyzer (red). This results in two waves with retardation  $\Delta$ , leading to the observed images due to interference.

the survey by Kratz et al. [KASH13] for further literature on tensor field visualization, and to the work by Kratz et al. [KSZ\*14] for a visualization-guided design study of a brake lever, which we also use for demonstrating our technique. The works most closely related to ours, in the sense that indefinite second-order symmetric tensor fields are visualized in a continuous manner with an optical model, are that by Kratz et al. [KMH11] and Dick et al. [DGBW09]. Both approaches involve raycasting but address goals different to ours—we aim at exploiting photoelasticity and, in particular, the experimental experience and knowledge on how photoelasticity is applied and interpreted.

### 3. Method

Section 3.1 gives an introduction to the functionality of polariscopes and provides basics, followed by a description of the stress-optic law in Section 3.2, which represents a simplified model for two-dimensional problems, i.e., where birefringence does not vary along light rays. This provides a basis for integrated photoelasticity (Section 3.3), as presented by Aben [Abe79]. In Section 3.4, we show how we extend the concept with refraction and reflection. In Section 4, we describe how the overall approach is integrated in the raycasting framework and provide implementation details.

#### 3.1. Polariscope Functionality

A polariscope consists of a plane light (Figure 2(a)), a linear polarization filter denoted “polarizer” (b), an optional  $\lambda/4$ -wave plate (c), the object to analyze (d), another optional  $\lambda/4$ -plate (e), another linear polarization filter denoted “analyzer” (f), and the observer or optical acquisition device (g).

In a circular polariscope, both  $\lambda/4$ -plates are present, whereas they are missing in a plane polariscope. A wave plate causes a retardation, i.e., a lower speed of light, on the light components oriented along its “slow” direction (blue arrows in Figure 2), whereas components along its “fast” direction are less retarded. This results in a phase shift of the slow component relative to the fast component. A  $\lambda/4$ -plate causes a phase shift of  $\pi/2$ , producing circularly polarized light from linearly polarized light. Hence, the linear

polarization filter (b) together with the wave plate (c) can be subsumed as a circular polarization filter (circular polarizer), and the wave plate (e) together with the analyzer (f) as a second circular polarization filter. In a circular polariscope, the two wave plates are oriented perpendicular, i.e., with opposite fast and slow directions.

If no object (d) is present in the polariscope, light is polarized linearly at the polarizer, transformed to circular polarization at the first wave plate, transformed back to linearly polarized light at the second wave plate (with same polarization direction as before entering the first wave plate), and has to pass the analyzer. If the orientation of the analyzer is perpendicular to that of the polarizer, all light is blocked by the analyzer. Otherwise, depending on the angle of orientation between polarizer and analyzer, a certain amount of light is passing and reaches the detector (g). In this regard, the two wave plates (in other words, the difference between a planar and a circular polariscope) do not have a substantial impact.

If, however, a transparent object, which exhibits birefringence, is positioned inside the polariscope (d), retardation due to the object is visualized. Polariscopes are applied to visualize weak birefringence, which causes retardation but does not cause noticeable double refraction, i.e., geometrically deviating rays, as would be the case, for example, in calcite. Weak birefringence is, in particular, caused by stresses in transparent material, with fast and slow directions aligned with the stress directions. If now such weak birefringence is caused by the object, there is a phase shift between the slow and the fast light component arriving at the analyzer, and the analyzer “cuts” a linearly polarized component from both parts, resulting in two superposed polarized light waves exiting the polariscope and reaching the sensor. These two light waves are subject to a relative phase shift  $\Delta$ , also denoted retardation in this context. These two light waves are subject to interference, and hence amplify or annihilate each other depending on the relation between  $\Delta$  and their wavelength, leading to interference colors (Figure 1(d)).

Parametrization of the polariscope can be achieved by adding/removing both wave plates, rotating the analyzer around the view axis, and by rotating the object, or analyzer/polarizer simultaneously. In our case of a virtual po-

lariscope, we can also adjust the stress-optic coefficient (see below) to control the visualization (Figure 7). Note that adjusting this coefficient corresponds to choosing different optical materials. This is particularly beneficial in configurations where the stresses would be insufficient or too high to provide expressive visualization with, e.g., glass as material.

### 3.2. Stress-Optic Law

If light passes orthogonally a thin plate of material located in the polariscope, if the birefringence properties of this material do not change along the light ray, and if one of the principal stresses is also perpendicular to the plate interface, then two-dimensional photoelasticity is applicable, and the relative phase shift  $\Delta$  at the observer can be obtained directly by the stress-optic law [DR78]:

$$\Delta = \frac{2\pi h}{\lambda} C(\sigma_1 - \sigma_2), \quad (1)$$

where  $\sigma_1$  and  $\sigma_2$ ,  $\sigma_1 \geq \sigma_2$ , are the first and secondary principal stresses in the 2D plane,  $h$  is the slices thickness, and  $\lambda$  is the wavelength of the incident light wave.  $C$  is the stress-optic coefficient, which relates the indices of refraction to the principal stresses:

$$\Delta n = n_2 - n_1 = C(\sigma_1 - \sigma_2). \quad (2)$$

The stress-optic law is also applicable if the plate is not aligned with the principal stresses, in which case the phase shift is induced by the secondary principal stresses  $\sigma'_1$  and  $\sigma'_2$ ,  $\sigma'_1 \geq \sigma'_2$ . The secondary principal stresses can be obtained by intersecting the stress ellipsoid, i.e., the ellipsoid having the principal stresses as semi-principal axes, with a plane that passes through the center of the ellipsoid and is perpendicular to the incident ray. The semi-principal axes of the resulting intersection ellipse represent the secondary principal stresses (Figure 13.1 in Dally and Riley [DR78]).

However, if the principal stress directions (or the index ellipsoid representing the orientation and relative magnitude of the resulting refractive indices) vary along the light ray, the stress-optic law is not applicable. Since this is, in general, the case in polariscope analysis, we need to follow the extended approach of integrated photoelasticity.

### 3.3. Integrated Photoelasticity

For our approach, we follow the model of integrated photoelasticity by Aben [Abe79], which takes into account arbitrary variation of stress along the path of light. It can be shown that the stress-optic law is a special case of the integrated photoelasticity model, if secondary principal stress directions are considered and if the birefringence properties of the material do not vary along the ray.

Aben models the propagation of a polarized light wave through a photoelastic medium under arbitrary stress as the

electric vector  $\mathbf{E} \in \mathbb{C}^2$  propagating in  $z$ -direction as:

$$\frac{d\mathbf{E}}{dz} = \mathbf{G}\mathbf{E}, \quad \text{with } \mathbf{E} = \begin{pmatrix} E_x \\ E_y \end{pmatrix}, \quad (3)$$

with

$$\mathbf{G} = -i\frac{2\pi}{\lambda} C \begin{bmatrix} \frac{1}{2}(\sigma'_{11} - \sigma'_{22}) & \sigma'_{12} \\ \sigma'_{12} & -\frac{1}{2}(\sigma'_{11} - \sigma'_{22}) \end{bmatrix}. \quad (4)$$

Here,  $\sigma'_{ij}$  are the secondary stresses, i.e., the stresses in the plane perpendicular to the propagation vector of the light wave. We obtain  $\sigma'$  by projecting the 3D stress tensor  $\mathbf{S}$  on that plane, spanned by two orthonormal vectors  $\mathbf{s}_0$  and  $\mathbf{t}_0$ :

$$\sigma' = \begin{pmatrix} \mathbf{s}_0^T \mathbf{S} \mathbf{s}_0 & \mathbf{s}_0^T \mathbf{S} \mathbf{t}_0 \\ \mathbf{t}_0^T \mathbf{S} \mathbf{s}_0 & \mathbf{t}_0^T \mathbf{S} \mathbf{t}_0 \end{pmatrix}. \quad (5)$$

The model assumes weak birefringence [Or51], i.e.,  $\Delta n \sim O(10^{-3})$ . In our experiments, we did not encounter a situation that would have required exceeding this level.

The model of integrated photoelasticity describes the light wave propagation through a stressed medium by means of a polarized light vector. Hence, we can use Jones calculus [JON41] to solve for the complete light transport from the light source, through polarizer, wave plate, weakly birefringent medium, the secondary wave plate, and the analyzer to the observer. The  $x$ - and  $y$ -component of the polarized light vector traveling along the  $z$ -axis can be written

$$\begin{pmatrix} E_x(t) \\ E_y(t) \end{pmatrix} = \begin{pmatrix} \tilde{E}_x e^{i\phi_x} \\ \tilde{E}_y e^{i\phi_y} \end{pmatrix} e^{i(kz - \omega t)}, \quad (6)$$

with plane wave equation  $e^{i(kz - \omega t)}$  and Jones vector  $(\tilde{E}_x e^{i\phi_x}, \tilde{E}_y e^{i\phi_y})^T$ . To determine the intensity per wavelength at the observer, we are only interested in the amplitude and relative phase shift of the light vector, which is encoded by the Jones vector. Along with Jones vectors, we make use of Jones matrices to describe the optical elements along the light path. The circular polariscope with polarizer and analyzer at angles  $\varphi$  and  $\vartheta$ , respectively, is described by

$$\mathbf{E} = \mathbf{A} \mathbf{R}_{-\pi/4} \mathbf{C} \mathbf{R}_{\pi/4} \mathbf{D}_o \int_z \mathbf{G}(s) ds \mathbf{D}_i \mathbf{R}_{\pi/4} \mathbf{C} \mathbf{R}_{-\pi/4} \mathbf{E}_p I_1, \quad (7)$$

with

$$\mathbf{E}_p = \begin{pmatrix} \sin(\varphi) \\ \cos(\varphi) \end{pmatrix}, \quad \mathbf{A} = \begin{pmatrix} \cos^2 \vartheta & \cos \vartheta \sin \vartheta \\ \sin \vartheta \cos \vartheta & \sin^2 \vartheta \end{pmatrix}, \quad (8)$$

$$\mathbf{C} = e^{i\frac{\pi}{4}} \begin{pmatrix} 1 & 0 \\ 0 & -i \end{pmatrix}, \quad \mathbf{R}_\theta = \begin{pmatrix} \cos \theta & -\sin \theta \\ \sin \theta & \cos \theta \end{pmatrix}, \quad (9)$$

$I_1$  being the intensity incident from the light source,  $\mathbf{E}_p$  the polarized light vector,  $\mathbf{A}$  the Jones matrix of the analyzer,  $\mathbf{C}$  a quarter-wave plate with horizontal fast axis,  $\mathbf{R}_\theta$  rotates the optical element, and  $\mathbf{D}_i$  and  $\mathbf{D}_o$  model Fresnel refraction (Section 3.4). The intensity of linearly polarized light leaving the analyzer and reaching the observer is

$$I = E_x \overline{E_x} + E_y \overline{E_y}. \quad (10)$$

Conceptually, one has to evaluate Equation 10 (i.e., integrate Equation 7) for all wavelengths to obtain, for the given ray, the spectrum.

### 3.4. Extension with Refraction and Reflection

To achieve better depth perception and obtain results that better reflect typical experimental configurations of object geometry and refractive indices, we extend Aben's model of integrated photoelasticity by refraction and reflection. Since both involve changes in the polarization of light, we make use of Jones calculus here, too.

Refraction and reflection is described by the Fresnel equations. When light is reaching a material interface from a medium with refractive index  $n_1$  to a medium with refractive index  $n_2$ , where the incident ray forms an angle  $\theta_i$  with the surface normal, part of it is generally reflected at angle  $\theta_r = \theta_i$ , while the remaining part is generally refracted into the second medium at angle  $\theta_t$  according to Snell's law:

$$\frac{\sin \theta_i}{\sin \theta_t} = \frac{n_2}{n_1}. \quad (11)$$

Fresnel's equations include a formulation in terms of power and one in terms of amplitude. Since we want to include refraction and reflection within the object, we need to use the amplitude formulation to be able to include it into the integrated photoelasticity approach in terms of retardation. Both the refracted and reflected rays are formulated in terms of (a superposition of)  $p$ -polarized and  $s$ -polarized light. For the incident ray, the component  $\mathbf{p}$  that is polarized in the incident plane (containing the incident ray, the surface normal, and the refracted ray), is denoted  $p$ -polarized, while its component  $\mathbf{s}$  polarized perpendicular to this plane is  $s$ -polarized. According to Fresnel, the reflected ray consists of an amount  $r_s$  of  $s$ -polarized light and amount  $r_p$  of  $p$ -polarized light, whereas the refracted ray consists of an amount  $t_s$  of  $s$ -polarized light and  $t_p$  of  $p$ -polarized, with

$$r_s = \frac{n_1 \cos \theta_i - n_2 \cos \theta_t}{n_1 \cos \theta_i + n_2 \cos \theta_t} \quad (12)$$

$$r_p = \frac{n_2 \cos \theta_i - n_1 \cos \theta_t}{n_1 \cos \theta_t + n_2 \cos \theta_i} \quad (13)$$

$$t_s = \frac{2n_1 \cos \theta_i}{n_1 \cos \theta_i + n_2 \cos \theta_t} \quad (14)$$

$$t_p = \frac{2n_1 \cos \theta_i}{n_1 \cos \theta_t + n_2 \cos \theta_i}. \quad (15)$$

As will be discussed in Section 4.1, we treat within the medium only total internal reflection, hence we need to apply Fresnel's equations only at the ray's entry and exit point. This is accomplished by integrating them into Equation 7

using the extended Jones matrix method [Yeh82]:

$$D_i = \begin{pmatrix} \mathbf{s} \cdot \mathbf{e} t_s & \mathbf{p} \cdot \mathbf{e} t_p \\ \mathbf{s} \cdot \mathbf{o} t_s & \mathbf{p} \cdot \mathbf{o} t_p \end{pmatrix}, D_o = \begin{pmatrix} \mathbf{e} \cdot \mathbf{s} t_s & \mathbf{o} \cdot \mathbf{s} t_s \\ \mathbf{e} \cdot \mathbf{p} t_p & \mathbf{o} \cdot \mathbf{p} t_p \end{pmatrix}, \quad (16)$$

where, in case of weak birefringence, as assumed,  $\mathbf{o}$  is perpendicular to  $\mathbf{s}$  and the refracted ray, while  $\mathbf{e}$  is perpendicular to  $\mathbf{o}$  and the refracted ray.

## 4. Implementation by Raycasting

We describe the implementation of the overall approach in terms of volumetric raycasting. We start with a description on how the rays are traced through the virtual polariscope (Section 4.1). Based on that, we give details on how photoelasticity is integrated (Section 4.2). Finally (Section 4.3), we describe how colors are obtained from Equation 10. Further details of our CUDA-based prototype are provided in the supplemental material accompanying this work.

### 4.1. Ray Traversal

We perform photoelasticity raycasting in the framework of traditional GPU-based front-to-back raycasting. The main reason for front-to-back order is not early ray termination (although we include absorption), it rather simplifies the handling and the implementation of photoelasticity integration. Due to Helmholtz reciprocity, reversing the direction of light transport holds also for photoelasticity.

Since we include reflection and refraction, intersections of the view ray with material interfaces have to be determined. We provide two approaches: either the whole dataset is assumed to exhibit uniform refractive index (Mode 1), or selected regions within the data can exhibit such a uniform refractive index (Mode 2). We assume vacuum in the surrounding volume. In our implementation, we do not consider continuous refraction (varying refractive index), however, it could be easily included, e.g., following the approach by Ament et al. [ABW14].

Overall, integration of reflection and refraction includes a raytracing problem. Nevertheless, we denote our approach raycasting-based because the focus is on the interaction with the medium, i.e., the integration of photoelasticity. We also model absorption to account for the absorption in physical materials. However, we omit emission in our results, although there might be applications, e.g., if luminescent materials are examined with a polariscope.

In our current implementation, we do not split rays at material interfaces to account for simultaneous reflection and refraction. Although this would be easily possible—the approach of integrated photoelasticity allows for superposition—we avoid it for several reasons:

- Light incident from the light source reflected at the material (case (i) in Figure 3) and reaching the camera

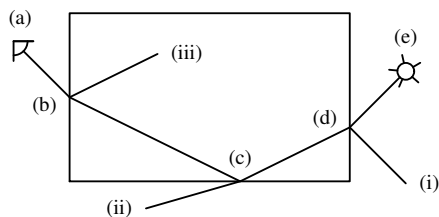


**Figure 3:** Illustration of ray traversal. Raycasting in direction from camera (a) to light source (e), but with reverse reflection/refraction, i.e., light direction is from (e) to (a).

would cause gloss and hinder proper analysis. Furthermore, since the light source in a polariscope is located behind the object, such gloss cannot appear. Hence, we do not need to split rays in this case. Nevertheless, we account for the loss (i) by applying the Fresnel equations at (d), regarding the intensity along (d)–(c).

- On the other hand, if light reaches the interface from inside the object, part of it can refract (ii) and hence exit, while part of it can be reflected to the interior ((c)–(b)). If there is total internal reflection, the ray does not need to be split. In this case we follow the ray. If, on the other hand, there is refraction, this can lead to two situations:
  - a) The exiting part reaches the camera ((b)–(a)). We handle this case directly by our front-to-back raycasting and account for the part that is lost due to internal reflection (iii) by applying the Fresnel equations at (b). However, we do not trace (iii) further, to ease the overall implementation, accelerate the overall technique, and avoid additional reflections which would further superimpose the patterns and complicate visual analysis. Nevertheless, integrating (iii) further would be a straightforward operation.
  - b) The exiting part does not reach the camera (ii). In this case, we stop the ray, i.e., we do not trace the internally reflected part ((c)–(b)) further, for the same reasons as in a). More precisely, both rays are ignored implicitly by our front-to-back raycasting approach.

As a consequence, during our front-to-back traversal, we test the Fresnel equations in reverse orientation (Figure 3(b)–(d)), i.e., if we are inside the medium, we test for reverse total internal reflection at each interface (e.g., (c), (d)). If there is reverse total internal reflection, we follow the reflected ray. If there is not total internal reflection, we exit the medium and test for intersection with the light source. If the plane light source is hit (e), our evaluation is complete. Otherwise, no light is contributed at the respective pixel.

In our present implementation, we either detect view ray intersections with the domain boundary (Mode 1), or provide a scalar field  $t$ , where the interface is defined implicitly (Mode 2), i.e., by an isosurface. In the raycasting kernel, we simply test for transition of the isolevel to determine the interface. The normal required for reflection and refraction is

provided by a vector field obtained from the gradient of  $t$  in a preprocessing step. For the shown results, we generated  $t$  by thresholding and subsequent smoothing. We have chosen this approach for its efficiency and ease of integration with existing raycasting code. Determining interface intersection and normals from meshes would be likewise possible.

## 4.2. Integration

We integrate photoelasticity by numerical integration of Equation 7 using the fourth-order Runge-Kutta scheme. Note that solving Equation 7 requires integration of a complex matrix. Finally, we prevent infinite integration due to total reflection by limiting the maximum number of bounces, 40 in our experiments. More details can again be found in the supplemental material.

## 4.3. Color Evaluation

In compliance with experimental polariscope analysis, we provide both chromatic and monochromatic operation. In the monochromatic case, Equation 10 is evaluated (and hence Equation 7 integrated) only once per view ray. For the chromatic results, we evaluated 16 [WND\*14] wavelengths, uniformly sampled in [380, 700] nm and converted the result using CIE31 to RGB color space.

## 5. Results

We start with a brief introduction to polariscope result interpretation in Section 5.1, followed by a short comparison to previous work (Section 5.2). Further introduction is provided in the supplemental material. We recommend to also watch the video [FM49] and to have a look at the polariscope analysis manual by Doyle and Phillips [Kob83]. Our first results visualize the Two-Point Load dataset (Section 5.3), followed by another simple dataset representing the setup from the video (Section 5.4). We then proceed to the Brake Lever dataset (Section 5.5), and conclude with the analysis of an anatomical simulation of a Femur (Section 5.6). Table 1 provides a subset of the timings obtained with a Nvidia GeForce GTX 760, which can be found in the supplemental material.

### 5.1. Polariscope Interpretation

The fringe patterns in Figure 4 exhibit areas, where extinction of light of a single wavelength occurs. Extinction happens where the secondary principal stresses differ by a factor of  $2\pi n$ ,  $n = 0, 1, 2, 3, \dots$ , causing isochromatic fringes that show loci with same order of relative retardation  $\Delta$  and hence similar stress. Starting from regions with no stress, the fringe order  $N$  is denoted  $N = \frac{\Delta}{2\pi}$ . Regions of high stress are revealed by close fringes. In a plane polariscope, the isochromatics are superimposed by isoclinic fringe patterns (e.g., the white vertical line in Figure 4(e)). These lines appear where the (rotated) stress directions coincide with the axis

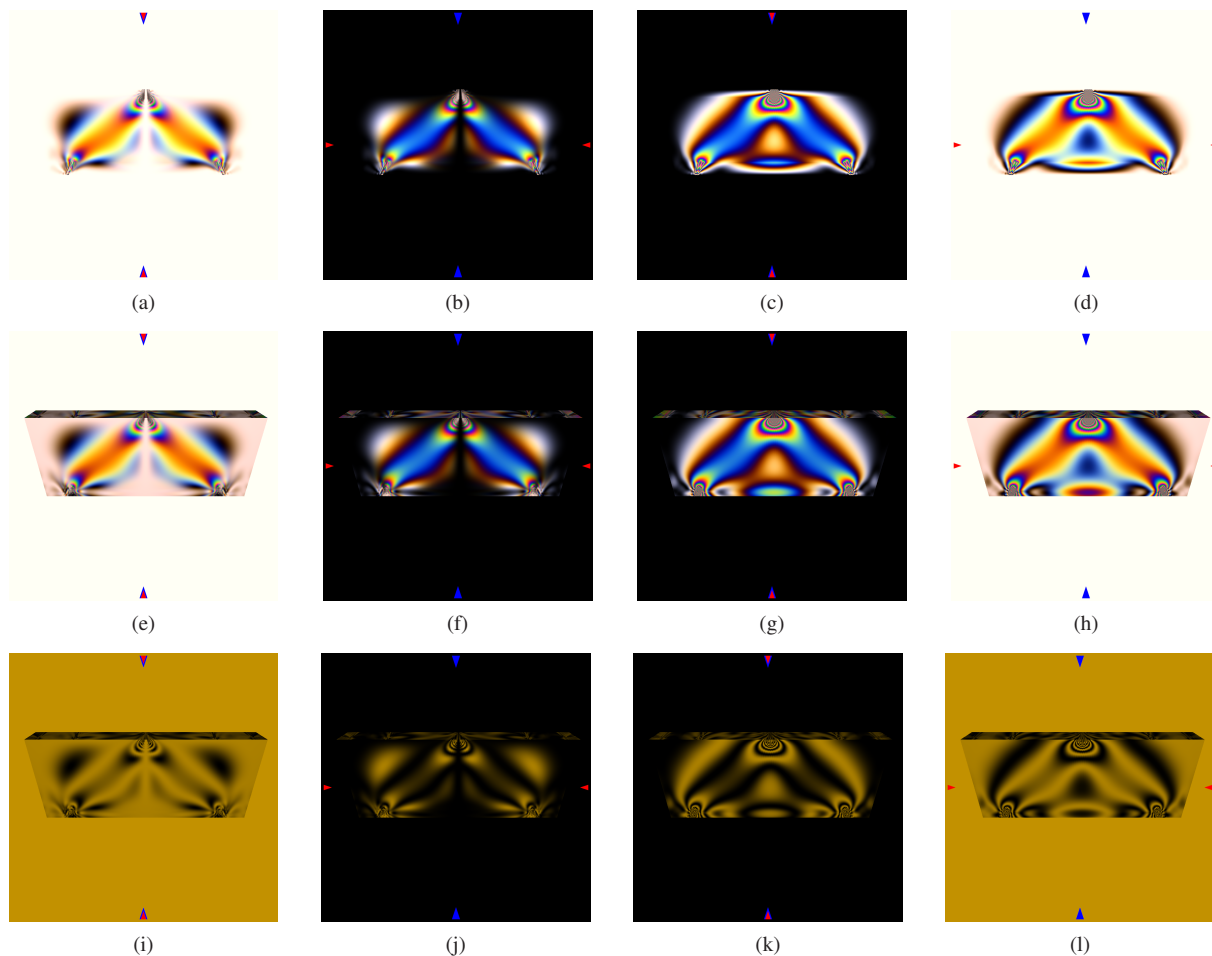


**Figure 4:** Simple Model dataset. Polarizer orientation by blue arrows, analyzer orientation by red arrows. No refraction/reflection (a)–(d), refraction/reflection (e)–(l), and monochromatic analysis (i)–(l) at 575 nm. Plane polariscope analysis (a), (b), (e), (f), (i), (j), and circular polariscope analysis (c), (d), (g), (h), (k), (l), with open (i.e., parallel) analyzer (left respective images) and closed (i.e., perpendicular) analyzer (right respective images).

of the polarizer. Hence, in experimental analysis with planar polariscopes, the polarizer can be rotated to identify stress orientation by means of isoclinic fringes. Circularly polarized light does not exhibit isoclinics, providing clear interpretation of isochromatics. Rotation of the object shows the fringe patterns from different perspectives and reveals the internal stress distribution. In this context, tensor field tomography based on 3D photoelasticity [WOH02] allows for estimation of internal stresses.

As described and compared with experiments by Aben, omitting refraction in our case corresponds to immersing the object under consideration in a liquid with identical refractive index to suppress refraction and reflection. However, as we show below, introducing refraction and reflection in most cases both improves depth perception and better reflects configurations that are achievable in real experiments.

For further details on polariscope interpretation, we would like to refer the reader to the related work in Section 2, the textbook by Doyle [Doy04], and our supplemental material for introductory examples on photoelastic analysis.

## 5.2. Polariscopes in Tensor Field Visualization

Figure 1 provides a comparison of different tensor field visualization techniques. We have chosen tensor field lines (Figure 1(a)) and tensor glyphs (Figure 1(b)), because they are widely used, volumetric raycasting of von Mises stress (Figure 1(c)) due to its physical relevance, and compare them to our virtual polariscope (Figure 1(d)). While tensor field lines provide continuous insight into the orientation of the stresses, they suffer from clutter and occlusion and do not reasonably convey the stress distribution and magnitude. Tensor glyphs (Figure 1(b)) show stress direction and give an

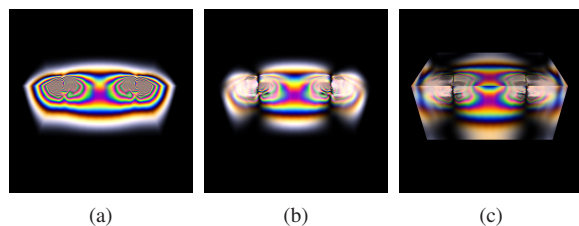


**Figure 5:** Two-Point Load dataset. (a) Circular photoelasticity raycasting without refraction. (b) Planar photoelasticity raycasting without refraction. (c) Planar photoelasticity raycasting with refraction (refractive index of 1.5).

overall impression of the distribution and magnitude of the internal stress. The major problem with glyphs we see here, however, is that they cannot provide a continuous picture, cannot span large ranges of magnitude, and are restricted to low resolutions due to occlusion and visual clutter. Von Mises volume rendering (Figure 1(c)) gives a more quantitative and physical view. However, as the stress tensor is represented by a scalar, directional information is lost. Polariscope analysis, on the other hand, provides a continuous representation, does not suffer from occlusion, and still conveys directions and even strong variations of stress.

### 5.3. Two-Point Load

We start with a simple dataset representing a block with two loads, one pushing, and one pulling. The data are given on a regular grid with a resolution of  $16 \times 16 \times 8$  nodes. For better insight, we visualize one half, cutting along the two loads. Figure 5 shows some results obtained with our technique. We start with a circular polariscope without refraction (Figure 5(a)). This shows the fringe pattern, but provides little insight with respect to depth or orientation. In Figure 5(b), we use the same setup for a plane polariscope. In this case, the dark isoclines show the circular structure of the stress field. Adding refraction (Figure 5(c)) improves depth perception, however, at the cost of distortions due to refraction, and mirroring due to reflection. Nevertheless, this represents the result that would also be observed in a real experiment.

### 5.4. Simple Model

This dataset was inspired by the video [FM49]. We recommend watching this video as an introduction to the topic, and, in particular, on how polariscopes are used. A corresponding finite element stress simulation was obtained (denoted Simple Model) and served for exemplary tests as well as for validation. The finite element simulation was carried out on a uniform grid with  $101 \times 41 \times 11$  nodes resolution and represents a homogeneous block of material supported at two positions and influenced by a load at its top, corresponding to the physical setup in the video (Figure 6(a)). A comparison with that frame from the video (Figure 6) shows

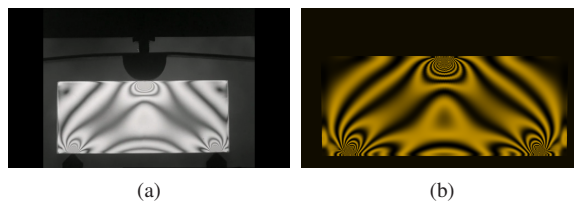


**Figure 6:** Experimental circular polariscope result (a) from [FM49], and our virtual circular polariscope result (b) for a corresponding stress simulation denoted Simple Model.

a reasonable fit between the experimental and our virtual polariscope. Figure 4 provides an overview of the different modes of our technique using this dataset.

### 5.5. Brake Lever

This dataset represents a stress simulation of a brake lever with a reinforcing rib structure. It consists of an unstructured grid containing 182036 tetrahedra, and provides a single time step of stress data. Since our implementation supports only uniform grids, we resampled the data on a regular grid with a resolution of  $120 \times 743 \times 365$  nodes, and provided a field for the implicit definition of the interface and one for the surface normals (Mode 2 of our technique). Figure 7(d) shows our result for stress-optic coefficient  $C = 50$  without refraction. In comparison with the corresponding result with refraction, shown in Figure 7(a), one can clearly see the benefit of refraction and reflection in photoelastic raycasting. Due to one's experience with transparent objects, depth perception is, overall, clearly improved. On the other hand, refraction and reflection can mislead interpretation. However, since our results reflect the real experiment, and support intuitive reasoning, we think that the overall advantages of using reflection and refraction are evident. Figures 7(e) and (b) show the same setup, but for the plane polariscope with the same overall trends. Figures 7(a), (c), and (f), finally show variation of the stress-optic coefficient. An interesting property of polariscope analysis is that even rather large values for  $C$  still produce well-interpretable visualizations due to the narrowing but still discernible fringe patterns.

### 5.6. Femur

The last dataset we apply our technique to, is an anatomical simulation of the stress in a Femur. The simulation consists of 33 time steps, each defined on a uniform grid of  $86 \times 81 \times 226$  nodes. The polariscope analysis shows the stress distribution from the top of the Femur and that the stresses mainly span along the outer wall of the bone. Figure 8 shows selected time steps, all with identical polariscope parametrization. We refer the reader to the supplemental material for the respective video, where we also demonstrate rotation of the analyzer to provide insight into the direction of the stresses.

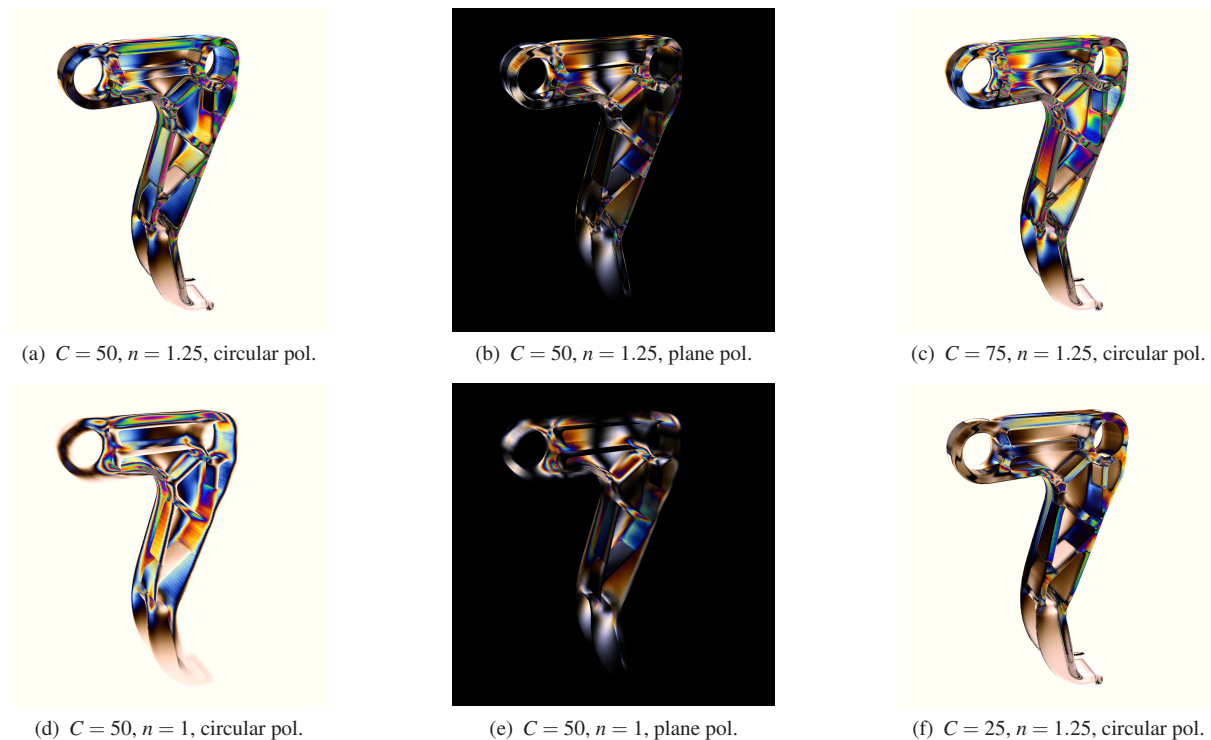


**Figure 7:** Brake Lever dataset for varying stress-optic coefficient  $C$  and refractive index  $n$ , circular and plane polariscope.

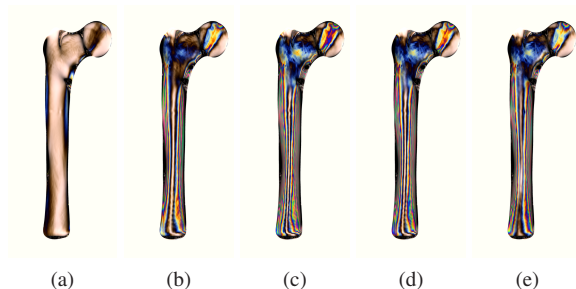


**Figure 8:** Selected time steps of Femur dataset, visualized with circular polariscope,  $C = 37$ , refractive index  $n = 1.3$ .

## 6. Conclusion

We have presented virtual polariscope visualization by integrating photoelasticity into the raycasting framework. For the integrated photoelasticity, we base our work on the approach by Aben [Abe79]. By employing the GPU, we are able to provide interactive analysis and, more important, we extend Aben's approach with reflection and refraction including Fresnel equations, providing a true counterpart to 3D polariscope analysis of arbitrarily-shaped objects. Our approach profits from the fact that experimental polariscope analysis has been applied since more than a century and, hence, is well understood. As future work, we plan to ex-

tend our approach to continuous refraction and would like to investigate polarization- and reflection/refraction-aware raycasting in other applications.

## Acknowledgements

We would like to thank Oliver Röhrle for simulating the Simple Model dataset, Gerik Scheuermann for the Two-Point Load dataset, Markus Stommel for the Brake Lever dataset, Christian Dick for the Femur dataset, and the German Research Foundation (DFG) for support of the project within the Cluster of Excellence in Simulation Technology (EXC 310/1) at the University of Stuttgart.

**Table 1:** Render timings in ms for the shown datasets. Interactive ( $1000^2$ ), vs. high-res resolution ( $2000^2$ ). Note that we provide preview rendering (reduced resolution, increased integration step, less wave length samples) during interaction, which achieved more than 60 fps in all experiments.

Dataset	Stepsize	Interactive	High-Res
Simple Model	$1 \times 10^{-2}$	624	2557
Two-Point Load	$1 \times 10^{-2}$	1113	6403
Femur	$5 \times 10^{-3}$	231	904
Brake Lever	$5 \times 10^{-3}$	363	1288

## References

- [Abe79] ABEN H.: *Integrated Photoelasticity*. Advanced book program. McGraw Hill International Book Company, 1979. 2, 3, 4, 9
- [ABW14] AMENT M., BERGMANN C., WEISKOPF D.: Refractive radiative transfer equation. *ACM Transactions on Graphics* 33, 2 (2014), 17:1–17:22. 5
- [Cha60] CHANDRASEKHAR S.: *Radiative Transfer*. Dover Books on Intermediate and Advanced Mathematics. Dover Publications, 1960. 2
- [DGBW09] DICK C., GEORGI J., BURBKART R., WESTERMANN R.: Stress tensor field visualization for implant planning in orthopedics. *IEEE Transactions on Visualization and Computer Graphics* 15, 6 (2009), 1399–1406. 3
- [DH93] DELMARCELLE T., HESSELINK L.: Visualizing second-order tensor fields with hyperstreamlines. *IEEE Computer Graphics and Applications* 13, 4 (1993), 25–33. 2
- [Doy04] DOYLE J. F.: *Modern Experimental Stress Analysis: Completing the Solution of Partially Specified Problems*. Wiley, Chichester, 2004. 7
- [DR78] DALLY J., RILEY W.: *Experimental Stress Analysis*. McGraw-Hill, 1978. 4
- [DWG\*06] DEUSCHLE H. M., WITTEL F. K., GERHARD H., BUSSE G., KRÖPLIN B.-H.: Investigation of progressive failure in composites by combined simulated and experimental photoelasticity. *Computational Materials Science* 38, 1 (2006), 1–8. 2
- [FM49] FÖPPL L., MÖNCH E.: Photoelasticity. Video, 1949. doi:10.3203/IWF/C-558. 2, 6, 8
- [Hec02] HECHT E.: *Optics*. Addison-Wesley, 2002. 2
- [JON41] JONES R. C.: A new calculus for the treatment of optical systems. *Journal of the Optical Society of America* 31, 7 (1941), 500–503. 4
- [KASH13] KRATZ A., AUER C., STOMMEL M., HOTZ I.: Visualization and analysis of second-order tensors: Moving beyond the symmetric positive-definite case. *Computer Graphics Forum - State of the Art Reports 1* (2013), 49–74. 3
- [KMH11] KRATZ A., MEYER B., HOTZ I.: A visual approach to analysis of stress tensor fields. In *Scientific Visualization: Interactions, Features, Metaphors*, vol. 2. 2011, pp. 188–211. 3
- [Kob83] KOBAYASHI A.: *Manual on Experimental Stress Analysis*. Society for Experimental Stress Analysis, 1983. 2, 6
- [KSZ\*14] KRATZ A., SCHOENEICH M., ZOBEL V., BURGETH B., SCHEUERMANN G., HOTZ I., STOMMEL M.: Tensor visualization driven mechanical component design. In *Proceedings of the IEEE Pacific Visualization Symposium* (2014), pp. 145–152. 3
- [KW99] KINDLMANN G., WEINSTEIN D.: Hue-balls and lit-tensors for direct volume rendering of diffusion tensor fields. In *Proceedings of the IEEE Conference on Visualization* (1999), pp. 183–189, 524. 2
- [LSG12] LATORRE P., SERON F., GUTIERREZ D.: Birefringence: calculation of refracted ray paths in biaxial crystals. *The Visual Computer* 28, 4 (2012), 341–356. 2
- [MHC93] MCCLAIN S. C., HILLMAN L. W., CHIPMAN R. A.: Polarization ray tracing in anisotropic optically active media. i. algorithms. *Journal of the Optical Society of America A* 10, 11 (1993), 2371–2382. 2
- [O'r51] O'ROURKE R.: Three-dimensional photoelasticity. *Journal of Applied Physics* 22, 7 (1951), 872–878. 4
- [Pat02] PATTERSON E. A.: Digital photoelasticity: Principles, practice and potential. *Strain* 38, 1 (2002), 27–39. 2
- [Sha08] SHARPE W.: *Springer Handbook of Experimental Solid Mechanics*. Springer, 2008. 2
- [SK10] SCHULTZ T., KINDLMANN G.: Superquadric glyphs for symmetric second-order tensors. *IEEE Transactions on Visualization and Computer Graphics* 16, 6 (2010), 1595–1604. 2
- [WK90] WOLFF L., KURLANDER D.: Ray tracing with polarization parameters. *IEEE Computer Graphics and Applications* 10, 6 (1990), 44–55. 2
- [WKL99] WEINSTEIN D. M., KINDLMANN G. L., LUNDBERG E. C.: Tensorlines: Advection-diffusion based propagation through diffusion tensor fields. In *Proceedings of the IEEE Conference on Visualization* (1999), pp. 249–253, 530. 2
- [WND\*14] WILKIE A., NAWAZ S., DROSKE M., WEIDLICH A., HANIKA J.: Hero wavelength spectral sampling. *Computer Graphics Forum* 33, 4 (2014), 123–131. 6
- [WOH02] WIJERATHNE M., OGUNI K., HORI M.: Tensor field tomography based on 3D photoelasticity. *Mechanics of Materials* 34, 9 (2002), 533–545. 7
- [WPG\*97] WESTIN C.-F., PELED S., GUDBJARTSSON H., KIKINIS R., JOLESZ F. A.: Geometrical diffusion measures for MRI from tensor basis analysis. In *Proceedings of the International Society for Magnetic Resonance in Medicine* (1997), p. 1742. 2
- [WTP01] WILKIE A., TOBLER R. F., PURGATHOFER W.: Combined rendering of polarization and fluorescence effects. In *Proceedings of the 12th Eurographics Workshop on Rendering Techniques* (2001), pp. 197–204. 2
- [WW08] WEIDLICH A., WILKIE A.: Realistic rendering of birefringency in uniaxial crystals. *ACM Transactions on Graphics* 27, 1 (2008), 6:1–6:12. 2
- [WW10] WILKIE A., WEIDLICH A.: A standardised polarisation visualisation for images. In *Proceedings of the 26th Spring Conference on Computer Graphics* (2010), pp. 43–50. 2
- [WW12] WILKIE A., WEIDLICH A.: Polarised light in computer graphics. In *SIGGRAPH Asia 2012 Courses* (2012), pp. 8:1–8:87. 2
- [Yeh82] YEH P.: Extended Jones matrix method. *Journal of the Optical Society of America* 72, 4 (1982), 507–513. 5